33rd Annual International Conference of the IEEE EMBS
Boston, Massachusetts USA, August 30 - September 3, 2011

Cubic Hermite Bezier Spline Based Reconstruction of Implanted Aortic Valve Stents from CT Images

Michael Gessat, Lukas Altwegg, Thomas Frauenfelder, André Plass, and Volkmar Falk

Abstract— **Mechanical forces and strain induced by transcatheter aortic valve implantation are usually named as origins for postoperative left ventricular arrhythmia associated with the technique. No quantitative data has been published so far to substantiate this common belief. As a first step towards quantitative analysis of the biomechanic situation at the aortic root after transapical aortic valve implantation, we present a spline-based method for reconstruction of the implanted stent from CT images and for locally measuring the deformation of the stent.**

I. INTRODUCTION

Transcatheter aortic valve implantation (TAVI) has evolved to be an important treatment option for high-risk patients with severe aortic stenosis (AS) and has helped to reduce the rate of untreated cases of AS [1]. Two devices are primarily in use, the Medtronic CorveValve Revalving System (MCRS) and the Edwards SAPIEN valve (ESV). A number of studies on large national and international registries has proven the efficacy of the method with respect to mortality in comparison to standard medical treatment of inoperable AS patients [2]–[4]. Besides vascular complications and other rare adverse events, left ventricular conductive abnormalities - mostly left bundle branch blocks (LBBB) and atrioventricular node blocks (AVB) - which require permanent pacemaker implantation are documented in the context of TAVI.

Incidence of new pacemaker dependency after transcatheter MCRS implantation is reported between 19% and 49% [4]–[8] (weighted mean $30\% \pm 7\%$) . Bosmans et al. [4] directly compared clinical data from 141 MCRS and 187 ESV cases treated at ten centers in Belgium and reported a significantly higher rate of new pacemakers in MCRS patients than in ESV patients (22% vs. 5%, $p < 0.001$). Several baseline clinical parameters have been reported to correlate with new pacemaker dependency after TAVI [5]–[7], [9]–[12]. Besides valve selection, the following procedure-related risk factors have been reported: valve sizing [11], [12], insertion depth [7], [12], and balloon predilatation [11].

M. Gessat is with the University Hospital Zrich, Division for Cardiovascular Surgery and with the Swiss Federal Institute of Technology (ETH), Computer Vision Laboratory, Zrich, Switzerland. gessat@vision.ee.ethz.ch

L. Altwegg is with the University Hospital Zürich, Division of Cardiology, Zürich, Switzerland. lukas.altwegg@usz.ch

T. Frauenfelder is with the University Hospital Zürich, Institute of Diagnostic and Interventional Radiology, Zürich, Switzerland. thomas.frauenfelder@usz.ch

A. Plass is with the University Hospital Zürich, Division for Cardiovascular Surgery, Zürich, Switzerland. andre.plass@usz.ch

V. Falk is with the University Hospital Zürich, Division for Cardiovascular Surgery, Zürich, Switzerland. volkmar.falk@usz.ch

Mechanical forces or strain induced on the interface between stent and tissue, in particular those in the vicinity of the atrioventricular node or the left bundle branch, are frequently named as an origin of observed AVBs and LBBBs [10], [13]. Nevertheless, no study provided any quantitative data on the magnitude of these forces. One reason for this is that by now, there is no mechanism to measure these forces or to estimate them based on biomechanical analysis.

The ultimate goal of our project group is to investigate the biomechanical situation at the interface between stent, tissue, and calcifications during and after TAVI. As a first step, we present in this paper a Bezier spline based method for reconstructing the shape of implanted MCRS stents from postoperative CT images and measuring the deformation of a MCRS stent in comparison to the (known) undeformed shape of the stent.

II. MATERIALS & METHODS

The MCRS consists of a nitinol stent and leaflets manufactured from porcine pericardial tissue. The superelastic properties of nitinol allow crimping of the stent to a small diameter for transcather implantation. During stent implantation, a sheath is retracted from the crimped stent, allowing it to unfold the leaflets inside the aortic root. Since the fully unfolded stent would be larger than the diameter of the aortic valve and the ascending aorta, the final shape of the stent is constituted by a balance of forces between the elastic forces from the stent trying to unfold and the surrounding tissues.

Fig. 1 shows the MCRS in a relaxed state and a volumetric representation of a postoperative CT image acquired from a patient after MCRS implantation. The aim of the presented work was to quantitatively describe the observerable deformation between the relaxed state and the implanted state. Like every spatial deformation, this deformation can be regarded as an inhomgeneous transformation applied to a vector space containing the stent. Based on a principal continuity assumption, a reasonably dense sampled vector field is regarded to be a feasible representation of this transformation. Such a vector field is created by creating surface models of the deformed and the undeformed stent, registering both models, and measuring the displacement of each surface point.

The MCRS stent has a scaffold-like structure which can be described by a set of 300 s-shaped wires which connect 165 intersection points arranged in sets of 15 points, each lying on one of 11 parallel circles of different radii. The intersection points are denoted as $\mathbf{p}_{ij} \in \mathbf{R}^3$ where $i \in [0, 10] \subset \mathbf{N}$ identifies the layer and $j \in \mathbf{Z}_{15}$ identifies

978-1-4244-4122-8/11/$26.00 ©2011 IEEE

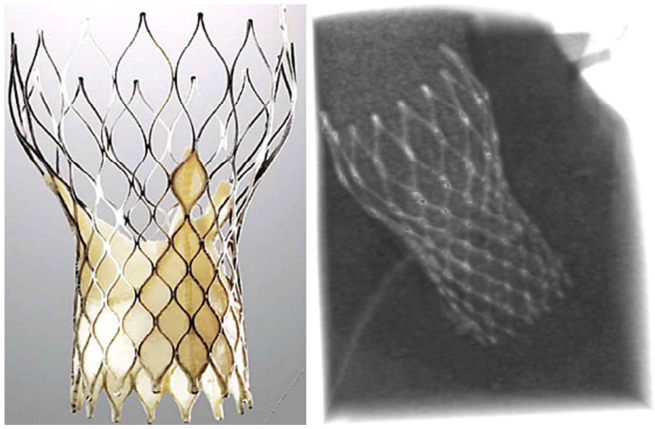

Fig. 1. Medtronic CoreValve before (left) and after (right) implantation.

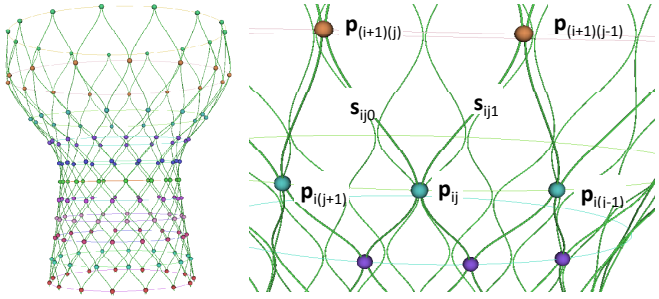

Fig. 2. The 165 intersection points on the stent centerlines. Right image shows indexing of points and curvelets in close-up view.

the position on the circle as shown in Fig. 2. The s-shaped piece of nitinol which connects the intersection points on layers 0 - 9 with their neighbours on the consecutive layers are represented by a s-shaped polynomial *curvlets* $\mathbf{s}_{ijk}$, with $k \in \mathbf{Z}_2$, also shown in Fig. 2. In the following we will describe the usage of cubic Bezier spline interpolation to define these curvelets in a way which assures that the resulting curves which run accross the intersection points are continuous and continuously derivable. The definition is made in a way which can be applied to the undeformed case represented by the 165 intersection points in their default position as well as to a deformed case represented by the intersection points as they are localized in postoperative CT images.

Based on third order Bernstein Polynomials $B_i^3(t) = \binom{3}{i} t^i (1-t)^{3-i}$ a third order Bezier curve is defined by four control points $\mathbf{b}_0, ..., \mathbf{b}_3 \in \mathbf{R}^3$: $\mathbf{b}(t) = \sum_i \mathbf{b}_i B_i^3(t)$ [14]. Among others, the curve has two important properties:

- $\mathbf{b}(0) = \mathbf{b}_0$ and $\mathbf{b}(1) = \mathbf{b}_3$ (endpoint interpolation)
- $\mathbf{b}'(0) = \mathbf{b}_1 - \mathbf{b}_0$ and $\mathbf{b}'(1) = \mathbf{b}_3 - \mathbf{b}_2$ (end-tangent interpolation)

A. Continuity Conditions

Across the 11 layers, the curvelets $\mathbf{s}_{ijk}$ are stiched together to splines $\mathbf{s}_{jk}$ with $k \in \{0, 1\}$ as follows: $\mathbf{s}_{jk} = \{\mathbf{s}_{0jk}, \mathbf{s}_{1j(k+1)}, \mathbf{s}_{2jk}, \ldots, \mathbf{s}_{10jk}\}$. In order to come to a smooth model of our stent, a control polygon for every curvelet $\mathbf{s}_{ijk}$ is constructed according to these conditions:

$$\begin{aligned} \mathbf{s}'_{ij0}(0) &= \mathbf{s}'_{ij1}(0) && (c1) \\ \mathbf{s}'_{ij0}(1) &= \mathbf{s}'_{(i+1)j1}(0) && (c2) \\ \mathbf{s}'_{ij1}(1) &= \mathbf{s}'_{(i+1)(j-1)0}(0) && (c3) \end{aligned}$$

B. Tangent Definition

The continuity conditions restrict neighbouring curvelets to a mutual tangent at the intersections points where they make contact. What is still missing is a heuristic to determine a direction for this mutual tangent. For this purpose, we need to take a closer look at the intersection points. In the undeformed case, the points $\mathbf{p}_{ij}$ on each level i lie on one perfectly planar circle C_i. The $\mathbf{p}_{ij}$ divide the circle C_i at equidistant angles of $24°$ with a $12°$ degree shift between neighbouring circles: $\alpha_{(2i)j} = 24° * j$ and $\alpha_{(2i+1)j} = 24° * j + 12°$, respectively.

On each circle C_i, an additional set of 15 target points $\mathbf{r}_{ij}$ is generated by shifting the intersection points by $12°$. We define the tangent $\mathbf{t}_{ij}$ in an intersection point $\mathbf{p}_{ij}$ to be parallel to the connection of the target points $\mathbf{r}_{(i-1)j}$ and $\mathbf{r}_{(i+1)j}$ for $i \in [1, 9]$. In the first (last) level, the tangents are defined to point directly to the corresponding target point at the second (second-last) level.

For the deformed case, the intersection points on one level do not necessarily lie on a circle, nor are the angle between neighbouring points with respect to any virtual circle center necessarily equal on a level. What we assume instead is that the points belonging to one level i lie on a reasonably smooth cyclic curve, which can be approximated by a second order Bezier spline $\mathbf{c}_i$ that interpolates the intersection points $\mathbf{p}_{ij}$. The spline is stiched together from 15 quadratic Bezier curves $\mathbf{c}_{ij}(t)$, $t \in [0, 1] \subset \mathbf{R}$, which are designed to be continuous and continuously derivable in the points $\mathbf{p}_{ij}$. In the style of the definition above, one can now calculate target points $\mathbf{r}_{ij} = \mathbf{c}_{ij}(0.5)$ for the deformed case and follow the construction above to define the tangents needed to define the Bezier curvelets $\mathbf{s}_{ijk}$.

C. Construction of Control Polygons

Based on the assumptions and definitions stated above, the control polygon of the curvelets $\mathbf{s}_{ijk}$ is constructed as follows: Let $\mathbf{b}_0 \ldots \mathbf{b}_3$ be the control polygon of one curvelet $\mathbf{s}_{ij0}$ with $i \in [1, 9]$. The endpoint interpolation property tells us that $\mathbf{b}_0 = \mathbf{p}_{ij}$ and $\mathbf{b}_3 = \mathbf{p}_{(i+1)j}$. The end-tangent interpolation property and the continuity conditions (c2) and (c3) constrain $\mathbf{b}_1$ to the line $\mathbf{b}_0 + \lambda_{ij} * \mathbf{t}_{ij}$ and $\mathbf{b}_2$ to the line $\mathbf{b}_3 - \lambda_{(i+1)j} * \mathbf{t}_{(i+1)j}$. With the Euclidian distances d between the intersection points to the target points above and below, we define

$$\lambda_{ij} = \frac{d(\mathbf{p}_{ij}, \mathbf{r}_{(i-1)j}) + d(\mathbf{p}_{ij}, \mathbf{r}_{(i+1)j})}{2} .$$

The control polygons and the resulting splines for a deformed case are shown in Fig. 3.

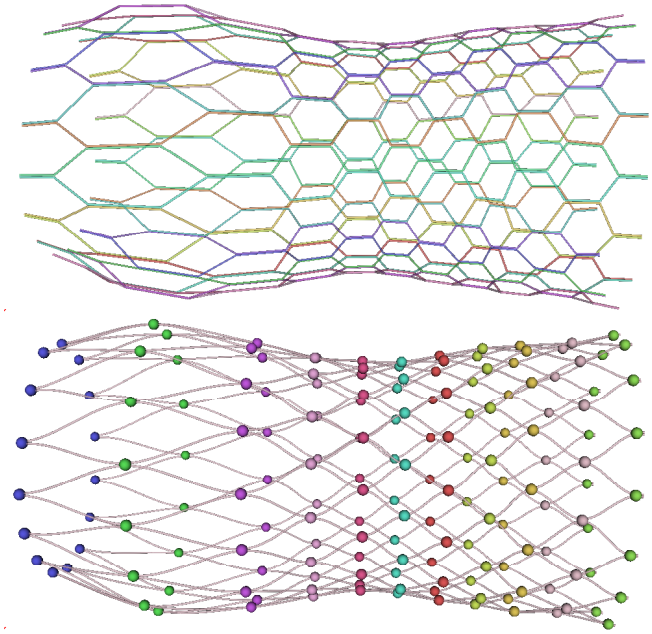

Fig. 3. Control polygons (above) and resulting splines (below) for a deformed case.

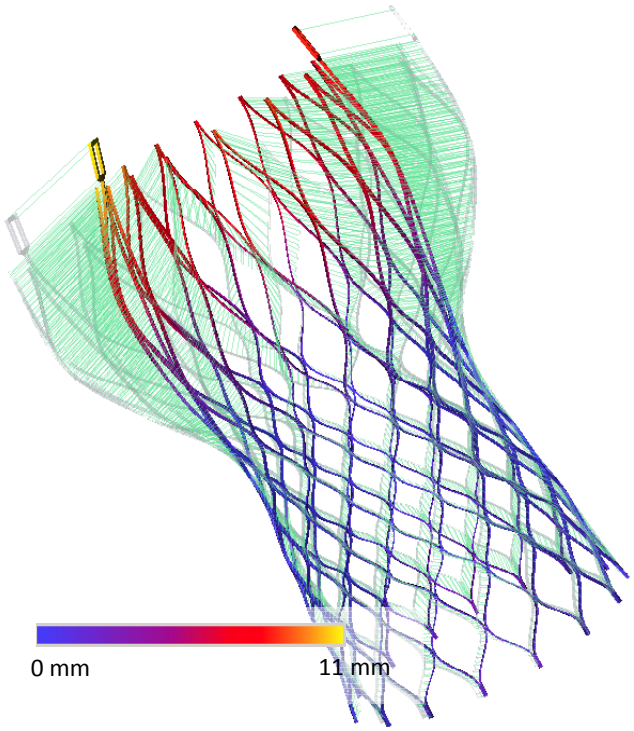

Fig. 4. Displacement of model points visualized as vector field (green lines, subsampled 1:100) and color-mapped magnitude.

D. Sampling and Wrapping of Splines

So far we have only discussed the generation of splines which approximate the centerlines of the wires which form the stent. To come to a surface model of the stent, we have to add some flesh to these bones by wrapping the splines with rectangular profiles. In order to do this, a slight adjustment is required to the spline definitions first: Since the wires do actually not intersect at the $\mathbf{p}_{ij}$ but rather touch each others, the control points at the intersections and thereby the splines themselves are moved away from each others by half the thickness of one wire. These adjustment needs to be reflected in the construction of the tangents and the control polygons, making everything a bit more complicated but does not change anything there in principle. With these adjustments made, all curvelets are uniformly sampled and linearly interpolated between the sampling points. A rectangular profile is then moved along each spline, defining four points on the surface for every sample. For rendering purposes, a triangular mesh strucuture is generated as the points are structured, wrapping every wire in a waterproof shell of triangles. At the intersection points, where two neighbouring wires come close, the mesh topology is adapted in order to connect the two wires. Finally, the two hooks at the distal end of the stent are added to the surface mesh.

E. Rigid Registration and Deformation Mapping

The two sets of intersection points used to construct the undeformed and the deformed model are by default not spatially aligned. In fact, we chose the coordinate system of the undeformed case so that the circle C_0 lies in the $x-y$ plane with the origin at its center. The origin and axes of the coordinate system in which the intersection points are defined are defined by the CT scanner used to acquire the images in which the points were identified. As a first means to compensate for this, Principal Component Analysis is applied to roughly aling both models before starting to compute the displacement between the models' points and searching for a rigid registration which minimizes this displacement.

The fact that both, the undeformed and the deformed model, are constructed using the same algorithm, the point correspondonce problem between both models is trivial. Given the undeformed model M_u with surface points $P_u = \{\mathbf{P}_{u0}, \ldots, \mathbf{P}_{un}\}$ and the deformed model M_d with surface points $P_d = \{\mathbf{P}_{d0}, \ldots, \mathbf{P}_{dn}\}$, the displacement of every $\mathbf{P}_{ui}$ equals the vector $\mathbf{V}_i = \mathbf{P}_{di} - \mathbf{P}_{ui}$.

With the pre-registration based on PCA as a starting point, we iteratively search for a rigid registration to apply to the deformed stent which minimizes the sum of squared distances over all surface points. After finding this registration, the residual displacement of each point is taken as its actual displacement as effect of the physical deformation of the stent as it is visualized in Fig. 4.

III. ACCURACY

The first question asked to a reconstruction method as we propose it, will always address its accuracy. As a ground truth for the undeformed case, we acquired a micro CT scan of a CoreValve stent under unloaded conditions, derived a isosurface model from the images, and computed the point-wise distance between this isosurface and our model. At

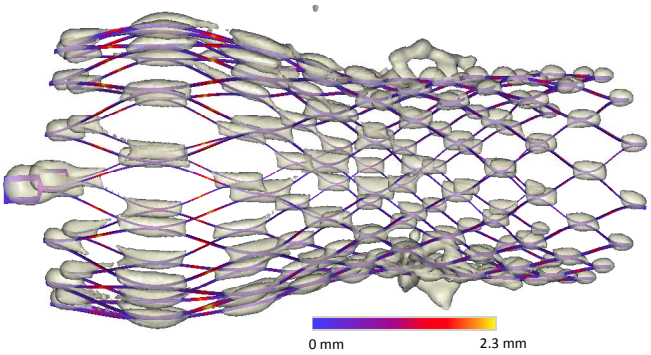

Fig. 5. Point-to-surface distance of reconstructed model to isosurface extracted from CT images. The missing parts, especially near the distal end of the stent, lead to large local overestimation of modelling error.

average, this distance was $0.18\,mm$ $(\pm 0.1\,mm)$, which is well below the image resolution we can aquire from patients and therefore regarded sufficient. For the deformed models, the quality of the available ground truth was limited to the image quality of the available postoperative patient scans. The spatial resolution of these scans was $0.4\,mm$. The partial volume effect which we encountered in the images plus the image artefacts caused by calcifications resulted in over- and undersegmentation artefacts in the reference surfaces. This lead to overestimation of the modelling error, as it can be seen in Fig. 5. Nevertheless, the resulting mean errors over a sample of 7 patient datasets did not exceed $0.6\,mm$ $(\pm 0.3\,mm)$.

IV. DISCUSSION AND CONCLUSION

The presented approach to measuring the deformation of implanted MCRS stents is a technical tool developed with the aim to be used in clinical research which will be conducted in subsequently. At present, we have applied the tool to seven patient cases, in which we were able to show that the extent as well as the pattern of deformation varies strongly between patients and has a potential influence on the onset of postoperative pacemaker requirement. We still have to learn how these deformation fields can help us in the future to understand the reasons for postoperative arrhythmia.

Future work will aim at correlating deformation patterns and magnitudes with clinically documented complications and at computation of the internal and external forces acting on the stent and, in the case of the external forces, the surrounding tissues based on the measured deformation. In addition, the method could be used in the future as a tool to evaluate simulation systems which try to predict the biomechanics of stent implantation.

V. ACKNOWLEDGMENTS

The authors gratefully acknowledge the contribution of National Research Organization and reviewers' comments. Medtronic, Inc. supported this work by providing two CoreValves for micro-CT acquisition. The project was financially supported by the Swiss Heart Foundation.

REFERENCES

[1] S. C. Malaisrie, E. Tuday, B. Lapin, E. Wang, R. Lee, E. C. McGee, C. Davidson, and P. M. McCarthy, "Transcatheter aortic valve implantation decreases the rate of unoperated aortic stenosis," *European Journal of Cardio-Thoracic Surgery: Official Journal of the European Association for Cardio-Thoracic Surgery*, Jan. 2011.

[2] M. B. Leon, C. R. Smith, M. Mack, D. C. Miller, J. W. Moses, L. G. Svensson, E. M. Tuzcu, J. G. Webb, G. P. Fontana, R. R. Makkar, *et al.*, "Transcatheter aortic-valve implantation for aortic stenosis in patients who cannot undergo surgery," *The New England Journal of Medicine*, vol. 363, no. 17, pp. 1597–1607, Oct. 2010.

[3] M. Thomas, G. Schymik, T. Walther, D. Himbert, T. Lefèvre, H. Treede, H. Eggebrecht, P. Rubino, I. Michev, R. Lange, *et al.*, "Thirty-day results of the SAPIEN aortic bioprosthesis european outcome (SOURCE) registry: A european registry of transcatheter aortic valve implantation using the edwards SAPIEN valve," *Circulation*, vol. 122, no. 1, pp. 62–69, July 2010.

[4] J. M. Bosmans, J. Kefer, B. D. Bruyne, P. Herijgers, C. Dubois, V. Legrand, S. Verheye, and I. Rodrigus, "Procedural, 30-day and one year outcome following CoreValve or edwards transcatheter aortic valve implantation: results of the belgian national registry," *Interactive Cardiovascular and Thoracic Surgery*, Feb. 2011.

[5] H. Jilaihawi, D. Chin, M. Vasa-Nicotera, M. Jeilan, T. Spyt, G. A. Ng, J. Bence, E. Logtens, and J. Kovac, "Predictors for permanent pacemaker requirement after transcatheter aortic valve implantation with the CoreValve bioprosthesis," *American Heart Journal*, vol. 157, no. 5, pp. 860–866, May 2009.

[6] P. Haworth, M. Behan, M. Khawaja, N. Hutchinson, A. de Belder, U. Trivedi, J. C. Laborde, and D. Hildick-Smith, "Predictors for permanent pacing after transcatheter aortic valve implantation," *Catheterization and Cardiovascular Interventions: Official Journal of the Society for Cardiac Angiography & Interventions*, vol. 76, no. 5, pp. 751–756, Nov. 2010.

[7] J. Baan Jr., Z. Y. Yong, K. T. Koch, J. P. Henriques, B. J. Bouma, M. M. Vis, R. Cocchieri, J. J. Piek, and B. A. de Mol, "Factors associated with cardiac conduction disorders and permanent pacemaker implantation after percutaneous aortic valve implantation with the CoreValve prosthesis," *American Heart Journal*, vol. 159, no. 3, pp. 497–503, 2010.

[8] C. Godino, F. Maisano, M. Montorfano, A. Latib, A. Chieffo, I. Michev, R. Al-Lamee, M. Bande, M. Mussardo, F. Arioli, *et al.*, "Outcomes after transcatheter aortic valve implantation with both Edwards-SAPIEN and CoreValve devices in a single center: the milan experience," *JACC. Cardiovascular Interventions*, vol. 3, no. 11, pp. 1110–1121, Nov. 2010.

[9] L. Roten, P. Wenaweser, E. Delacrétaz, G. Hellige, S. Stortecky, H. Tanner, T. Pilgrim, A. Kadner, B. Eberle, M. Zwahlen, *et al.*, "Incidence and predictors of atrioventricular conduction impairment after transcatheter aortic valve implantation," *The American Journal of Cardiology*, vol. 106, no. 10, pp. 1473–1480, Nov. 2010.

[10] C. Fraccaro, G. Buja, G. Tarantini, V. Gasparetto, L. Leoni, R. Razzolini, D. Corrado, R. Bonato, C. Basso, G. Thiene, *et al.*, "Incidence, predictors, and outcome of conduction disorders after transcatheter self-expandable aortic valve implantation," *The American Journal of Cardiology*, vol. 107, no. 5, pp. 747–754, Mar. 2011.

[11] M. Z. Khawaja, R. Rajani, A. Cook, A. Khavandi, A. Moynagh, S. Chowdhary, M. S. Spence, S. Brown, S. Q. Khan, N. Walker, *et al.*, "Permanent pacemaker insertion after CoreValve transcatheter aortic valve implantation: Incidence and contributing factors (the UK CoreValve collaborative)," *Circulation*, Feb. 2011.

[12] M. Gutiérrez, J. Rodés-Cabau, R. Bagur, D. Doyle, R. DeLarochellière, S. Bergeron, J. Lemieux, J. Villeneuve, M. Côté, O. F. Bertrand, *et al.*, "Electrocardiographic changes and clinical outcomes after transapical aortic valve implantation," *American Heart Journal*, vol. 158, no. 2, pp. 302–308, Aug. 2009.

[13] A. Sinhal, L. Altwegg, S. Pasupati, K. H. Humphries, M. Allard, P. Martin, A. Cheung, J. Ye, C. Kerr, S. V. Lichtenstein, and J. G. Webb, "Atrioventricular block after transcatheter balloon expandable aortic valve implantation," *JACC. Cardiovascular Interventions*, vol. 1, no. 3, pp. 305–309, June 2008.

[14] G. Farin, *Curves and Surfaces for CAGD. A practical guide.*, 5th ed. Academic Press, San Diego, 2002.